

PAPER

# Simulation of the hydrodynamic expansion following a nanosecond pulsed spark discharge in air at atmospheric pressure

To cite this article: Fabien Tholin and Anne Bourdon 2013 *J. Phys. D: Appl. Phys.* **46** 365205

View the [article online](#) for updates and enhancements.

## Related content

- [Simulation of the stable 'quasi-periodic' glow regime of a nanosecond repetitively pulsed discharge in air at atmospheric pressure](#)  
Fabien Tholin and Anne Bourdon
- [Influence of the external electrical circuit on the regimes of a nanosecond repetitively pulsed discharge in air at atmospheric pressure](#)  
Fabien Tholin and Anne Bourdon
- [Influence of temperature on the glow regime of a discharge in air at atmospheric pressure between two point electrodes](#)  
Fabien Tholin and Anne Bourdon

## Recent citations

- [Fully coupled modeling of nanosecond pulsed plasma assisted combustion ignition](#)  
Ashish Sharma *et al*
- [Guided ionization waves: The physics of repeatability](#)  
XinPei Lu and Kostya (Ken) Ostrikov
- [High-Energy Emissions Induced by Air Density Fluctuations of Discharges](#)  
C. Köhn *et al*



**IOP | ebooks™**

Bringing you innovative digital publishing with leading voices to create your essential collection of books in STEM research.

Start exploring the collection - download the first chapter of every title for free.

# Simulation of the hydrodynamic expansion following a nanosecond pulsed spark discharge in air at atmospheric pressure

Fabien Tholin<sup>1,2</sup> and Anne Bourdon<sup>1,2</sup>

<sup>1</sup> CNRS, UPR 288 'Laboratoire d'Energétique Moléculaire et Macroscopique, Combustion', Grande voie des vignes, 92295 Châtenay-Malabry, France

<sup>2</sup> Ecole Centrale Paris, Grande voie des vignes, 92295 Châtenay-Malabry, France

E-mail: [fabien.tholin@ecp.fr](mailto:fabien.tholin@ecp.fr) and [anne.bourdon@ecp.fr](mailto:anne.bourdon@ecp.fr)

Received 19 April 2013, in final form 5 July 2013

Published 22 August 2013

Online at [stacks.iop.org/JPhysD/46/365205](http://stacks.iop.org/JPhysD/46/365205)

## Abstract

This paper presents 2D simulations of the dynamics of formation of a nanosecond spark discharge between two point electrodes in air at atmospheric pressure at 300 and 1000 K, the induced air heating and the following hydrodynamic expansion. As a first step, we have considered that 30% of the discharge energy instantaneously heats the ambient air. At the end of the voltage pulse, it is shown that the energy density and the air temperature distributions are non-uniform in the interelectrode gap. Rapidly after the nanosecond voltage pulse, a cylindrical shock wave is formed and propagates with a velocity very close to the speed of sound of the surrounding ambient air. Furthermore, the rapid dilatation of the hot channel formed on the discharge path is observed for  $t \leq 1 \mu\text{s}$ , as in experiments. Then we have carried out a parametric study on the influence of the value of the fraction of discharge energy going to fast heating on the hydrodynamic expansion at 1000 K, assuming an instantaneously fast gas heating. For all values in the range of 15% to 60% studied in this work, we have observed a very similar gas dynamics. Then, we have considered that the nanosecond spark discharge heats the ambient air at 1000 K with a longer relaxation time of  $1 \mu\text{s}$ , and in this case we have observed the propagation of a weak pressure wave and no dilatation of the hot channel on the discharge path. Finally, the comparison with experiments seems to validate the hypothesis that the 10 ns spark discharges studied in this work at 300 and 1000 K, significantly heat the ambient air on very short time-scales.

(Some figures may appear in colour only in the online journal)

## 1. Introduction

Nanosecond repetitively pulsed (NRP) discharges are being increasingly studied for various applications such as plasma-assisted combustion (Pilla *et al* 2006, Starikovskaia 2006), aerodynamic flow control (Starikovskii *et al* 2009) or nanomaterial synthesis (Pai 2011). In these discharges, the application of high-voltage pulses generates a high electric field that allows an efficient electron impact ionization and the production of highly reactive species. Furthermore, a voltage pulse with a duration of a few nanoseconds is chosen to

ensure a low power consumption. Finally, the use of repetitive voltage pulses results in the accumulation of metastable species important for sustaining the discharge and active species interesting for applications.

Pai *et al* (2010a) have carried out a detailed experimental study to identify the different regimes of NRP discharges in air at atmospheric pressure in the temperature range 300 to 1000 K between two metallic point electrodes with a radius of curvature of about  $200 \mu\text{m}$ , for a gap size in the range 5–10 mm, for 10 ns voltage pulses with an amplitude in the range 5–10 kV and a repetition frequency in the range 1–30 kHz, and with

an external flow aligned with the axis of electrodes at  $0.5\text{--}2.6\text{ m s}^{-1}$ . It is interesting to note that the cumulative effect of repeated pulsing achieves a stable ‘quasi-periodic’ behaviour. Thus, even though they are transient, the NRP discharges have a visual resemblance with dc discharges. Three different discharge regimes have been observed as the applied voltage increases: corona, glow and spark regimes. It is interesting to note that corona and spark discharge regimes were easily obtained under almost all experimental conditions, whereas the glow regime existed only over a limited range of conditions between 750 and 1000 K. In Pai *et al* (2009), Rusterholtz (2012), Tholin and Bourdon (2011), Tholin and Bourdon (2013), experiments and simulations have been carried out to extend the domain of existence of the glow regime between two point electrodes in air at atmospheric pressure down to 300 K in varying the gap size, the radius of curvature of electrodes, the applied voltage and the external air flow.

Pai *et al* (2010b) have carried out an extensive experimental study of the spark regime of NRP discharges in air at atmospheric pressure in the temperature range 300 to 1000 K between two metallic point electrodes with a radius of curvature of about  $200\text{ }\mu\text{m}$ , for a gap size of 5 mm, for 10 ns voltage pulses with an amplitude up to 10 kV and a repetition frequency in the range 1–30 kHz, and with an external flow aligned with the axis of electrodes at  $0.5\text{--}2.6\text{ m s}^{-1}$ . The nanosecond spark discharge regime is characterized by an intense emission, a high conduction current and a significant heating of the gas (by about 1000 K (Pai *et al* 2010b, Rusterholtz *et al* 2012)) within a few tens of nanoseconds following each voltage pulse. Indeed, during a nanosecond discharge, a significant part of the discharge energy is used to produce vibrationally excited molecules and electronically excited atoms and molecules. In the literature, these last years, several works (Popov 2001, Naidis 2008, Aleksandrov 2010, Popov 2011a, 2011b, Mintoussou *et al* 2011, Rusterholtz *et al* 2012, Rusterholtz 2012) have been devoted to the study of the fast relaxation of the energy stored in the different internal modes of molecules and atoms in air and the subsequent rapid increase of the translational temperature of the neutral gas. As initially proposed by Popov (2001), an important process for fast gas heating in air at atmospheric pressure by nanosecond pulsed discharges seems to be the fast quenching of electronic excited levels of nitrogen in the so-called two-step mechanism. First, during the nanosecond voltage pulse, electronically excited nitrogen molecules are produced by electron impact due to the high electric field present in the discharge. In a second step, these molecules are quenched by neutral particles and mainly by  $\text{O}_2$  molecules. These quenching reactions are very efficient and occur quickly after the discharge in less than a few tens of nanoseconds (Rusterholtz *et al* 2012). As a consequence,  $\text{O}_2$  molecules are dissociated and part of the energy stored in the electronic excited levels of nitrogen molecules is transferred into kinetic energy of the oxygen atoms produced. In a few collisions, these oxygen atoms thermalize and then increase the neutral gas temperature.

Recently, in Xu *et al* (2011) single-shot schlieren images of NRP discharges between two point electrodes in air at atmospheric pressure in the temperature range 300 to 1000 K

starting from 50 ns after the discharge pulse were recorded. These images clearly show a shock wave propagation and the expansion of the heated gas channel formed on the discharge path. Then, the significant fast gas heating is believed to play a key role in the application of NRP spark discharges for aerodynamic flow control (Bityurin *et al* 2008, Starikovskii *et al* 2009) and plasma-assisted combustion (Pilla *et al* 2006, Starikovskaia 2006).

It is interesting to note that the gas heating following a dc spark in air at atmospheric pressure has been extensively studied experimentally (Maly 1984, Marode 1975a) and numerically, mostly in 0D and 1D (Marode 1975b, Marode *et al* 1979, Bastien and Marode 1985, Naidis 1999, Naidis 2005, Rioussset 2010). However, so far, only few studies have been devoted to the simulation of NRP discharges in the spark regime. In particular, Popov (2011b) has simulated in 1D the production of active species and the neutral gas temperature evolution during and after an NRP spark discharge voltage pulse and Naidis (2008) has simulated in 0D the multi-pulse nanosecond spark dynamics and the neutral gas temperature evolution after several voltage pulses. In this work, we propose to simulate in 2D the formation of a nanosecond spark between two point electrodes in air at atmospheric pressure, the fast gas heating during and after the voltage pulse and the following hydrodynamic expansion. We propose to compare our simulation results with experimental results obtained in Xu *et al* (2011) on the shock wave propagation and on the expansion of the heated gas channel formed on the discharge path.

In section 2.1, we present the equations needed for the numerical simulation of air streamer discharges at atmospheric pressure in a point-to-point geometry during a nanosecond voltage pulse. In section 2.2, we set out the model for the spark phase. In section 2.3, we present the model for the hydrodynamic expansion after the voltage pulse. In section 3.1 we simulate a nanosecond spark in air at 1000 K, the fast gas heating and the hydrodynamic expansion after the voltage pulse and simulation results are compared with experimental results obtained in Xu *et al* (2011). In sections 3.2 and 3.3 we carry out a parametric study on the fast gas heating source term and its relaxation time to study its influence on the hydrodynamic expansion observed after the voltage pulse. Finally, in section 3.4, we go into the results obtained for the simulation of a nanosecond spark in air at 300 K with fast gas heating and compare with experimental results obtained in Xu *et al* (2011).

## 2. Model formulation

### 2.1. Model for the streamer phase of the discharge during the voltage pulse

As shown in our previous numerical studies (Celestin *et al* 2009, Bourdon *et al* 2010, Tholin and Bourdon 2011, Tholin and Bourdon 2013) and validated by comparison with experiments in Tholin *et al* (2011), the discharge during a nanosecond voltage pulse between two point electrodes consists of a positive streamer propagating from the anode

to the cathode and a negative streamer propagating in the opposite direction until they impact each other to form a plasma channel. The most common and effective model to study streamer dynamics in air at atmospheric pressure is based on the following drift–diffusion equations for electrons, positive and negative ions coupled with Poisson’s equation (e.g. Kulikovsky 1997):

$$\begin{aligned}\partial_t n_e - \nabla \cdot (n_e \mu_e \mathbf{E} + D_e \nabla n_e) &= S_e + S_{ph} \\ \partial_t n_n - \nabla \cdot (n_n \mu_n \mathbf{E} + D_n \nabla n_n) &= S_n \\ \partial_t n_p + \nabla \cdot (n_p \mu_p \mathbf{E} - D_p \nabla n_p) &= S_p + S_{ph}, \\ \nabla^2 V &= -\frac{q_e}{\epsilon_0} (n_p - n_n - n_e)\end{aligned}\quad (1)$$

where subscripts ‘e’, ‘p’ and ‘n’ refer to electrons, positive and negative ions, respectively,  $n_i$  is the number density of species  $i$ ,  $V$  is the potential,  $\mathbf{E} = -\nabla V$  is the electric field,  $D_i$  and  $\mu_i$  are the diffusion coefficient and the absolute value of the mobility of species  $i$ , respectively,  $q_e$  is the absolute value of electron charge, and  $\epsilon_0$  is the permittivity of free space.  $S_{ph}$  is the photoionization source term and the  $S_i$  terms stand for the source terms of species  $i$  due to ionization, attachment, recombination and detachment processes.

We study axisymmetric streamers propagating between two aligned point electrodes and thus cylindrical coordinates  $(x, r)$ , are used with the  $x$ -axis as axis of the discharge. In this work, simulation results are presented for point-to-point configurations with hyperboloid electrodes with a radius of curvature of  $R_p = 300 \mu\text{m}$ . In Xu *et al* (2011), the point electrodes are separated by an adjustable distance of 2–4 mm and in this work, we have considered a 2.5 mm gap. For all discharge simulations, a computational domain with a radius of  $R_{\text{max}} = 1.0 \text{ cm}$  and a length  $L_{\text{max}} = 1.0 \text{ cm}$  is used with a fixed no-uniform rectilinear grid defined as in Tholin and Bourdon (2011).

In this work, we study the discharge dynamics at atmospheric pressure between two points in ambient air at  $T_g = 300 \text{ K}$  and in preheated air at  $T_g = 1000 \text{ K}$ . In the charged species transport equations, all transport coefficients and rate coefficients in source terms are assumed to be functions of the local reduced electric field  $E/N$ , where  $E$  is the electric field magnitude and  $N$  is the air neutral density. At  $T_g = 300 \text{ K}$ , all transport parameters for charged species are taken from Morrow and Lowke (1997) except diffusion coefficients for ions which are derived from mobilities using Einstein relation. Reaction rate coefficients for ionization, attachment and recombination processes are taken from Morrow and Lowke (1997). For detachment, as in Benilov and Naidis (2003), we use the detachment rate coefficient proposed by Mnatsakanyan and Naidis (1985) which is a function of the air temperature and the electric field. For photoionization, the three-group SP<sub>3</sub> model is used (Bourdon *et al* 2007) with boundary conditions given in Liu *et al* (2007). As discussed in our previous works (Celestin *et al* 2009, Bourdon *et al* 2010, Tholin and Bourdon 2011, Tholin and Bourdon 2013), to take into account the fact that the discharge occurs at atmospheric pressure at  $T_g = 1000 \text{ K}$ , we have only scaled the value of the total air

density:  $N_{1000} = 0.3 \times N_{300}$  where  $N_{300} = 2.45 \times 10^{19} \text{ cm}^{-3}$  is the density of air at 300 K. The decrease of the total density by a factor of 3.3 as the temperature increases from 300 to 1000 K, increases by the same factor the local reduced electric field  $E/N$  and then has a direct impact on transport parameters and reaction rates for air.

The charged species transport equations are solved using a modified 1D Scharfetter–Gummel algorithm (Kulikovsky 1995) with the parameter of this scheme,  $\epsilon_{\text{ISG}} = 10^{-2}$ . To simulate 2D discharges, we split the numerical resolution into two 1D problems in the  $x$  and  $r$  directions, respectively and we alternate the order of the resolution between  $x$  and  $r$  axes at each time-step. In this work, as in Celestin *et al* (2009) we take into account simplified boundary conditions: near the anode and cathode surfaces, gradients of electron density are assumed to be zero. The ghost fluid method is used to take into account the exact shapes of the electrodes in the resolution of Poisson’s equation on a rectilinear grid (Celestin *et al* 2009). The finite difference form of Poisson’s equation is solved using the SuperLU solver (Demmel *et al* 1999) (<http://crd.lbl.gov/xiaoye/SuperLU/>) with Dirichlet boundary conditions on electrodes and Neumann boundary conditions on the other axial and radial boundaries of the computational domain. For the time integration during the voltage pulse, a simple first-order Euler time integration is used for fluxes and the photoionization source term, and an explicit fourth order Runge–Kutta method (Ferziger and Peric 2002) is used for other source terms. For stability and accuracy, the time-step in our explicit simulations is limited by several considerations. The time-scales of relevance are the Courant  $\delta t_c$  time-scale, defined as in Vitello *et al* (1994), the chemistry time-scale  $\delta t_S$  due to ionization, attachment, recombination and detachment processes, and the dielectric relaxation time-scale  $\delta t_D = \epsilon_0 / (q_e \sum_i |n_i \mu_i|)$ . The model time-step is calculated as  $\delta t = \min(A_c \delta t_c, A_S \delta t_S, A_D \delta t_D, 10^{-10})$  with  $A_c = 0.5$ ,  $A_S = 0.05$  and  $A_D = 0.5$ . The upper limit value of  $10^{-10} \text{ s}$  is used as a characteristic time-step to follow accurately the time evolution of the nanosecond applied voltage.

For the voltage pulse, we model the whole shape of the nanosecond applied voltage pulse with a steep nanosecond voltage rise, voltage plateau and a steep nanosecond voltage decrease, as detailed in section 3.1 at  $T_g = 1000 \text{ K}$  and section 3.4 at 300 K. In the following, the value of the voltage plateau is referred to as the applied voltage. As initial condition, we consider a low uniform preionization of ambient air with  $10^4 \text{ cm}^{-3}$  electrons and positive ions as discussed in Pancheshnyi (2005). Finally, we compute the conductive current  $I$  and the total energy density  $e_J(t)$  of the discharge at time  $t$  from:

$$I = \int_S \mathbf{j}_c \cdot d\mathbf{S}, \quad (2)$$

and

$$e_J(t) = \int_0^t \mathbf{j}_c \cdot \mathbf{E} dt, \quad (3)$$

where  $\mathbf{j}_c$  is the conductive current density and  $S$  is a surface described by equation  $\{x = \text{Const}\}$ . The choice of the location of the surface  $S$  will be discussed in section 3.1.



## 2.2. Model for the spark phase of the discharge during the voltage pulse

In Tholin and Bourdon (2011), it has been shown that after the connection of both streamer discharges, the electric field in the plasma channel between point electrodes becomes rapidly rather uniform and equal to the average electric field (i.e. the applied voltage divided by the gap length). If the value of the average electric field is higher than the breakdown field, the electron density goes on increasing while the electric field remains constant and the discharge transits to a spark phase. This results in a very fast increase of the conductive current and of the energy released in the discharge. As the electron density increases in the spark phase, the dielectric relaxation time of the plasma  $\delta t_D$  decreases to values of the order of  $10^{-16}$  s, i.e. much less than the other characteristic time-scales of relevance for the selection of the explicit simulation time-step as explained in section 2.1. With such small time-steps, it is very time consuming to simulate the spark phase of a nanosecond pulsed discharge with the fluid model and the explicit numerical method described in section 2.1. However, it is important to note that during the spark phase the electric field remains rather constant and the chemistry of charged species is much slower than in the streamer phase. In fact, the severe time-step limitation is due to thin non-neutral regions close to electrodes and on the wings of the discharge channel.

As mentioned in the introduction, so far, only few studies have been devoted to the simulation of NRP discharges in the spark regime (Popov 2011b, Naidis 2008). In both studies, it is assumed that the electric field is uniform over the cross-section of the discharge channel and is either constant or derived from an experimental current distribution. In this work, in order to simulate the nanosecond spark discharge in 2D, we have used as a first step a simple approach, that we validate *a posteriori* by comparison of simulation results with experimental results in section 3. We have assumed that after the connection, the structure of the nanosecond spark discharge remains the same and that the electric field in the spark phase is proportional to the applied voltage. As a consequence, the space charge density  $\rho_c = q_e(n_p - n_n - n_e)$  has to evolve proportionally to the applied voltage during the spark phase:

$$\rho_c(t) = AV(t) \quad (4)$$

where  $V(t)$  is the applied voltage and  $A$  is a constant. It is reasonable to assume that only electrons have a sufficiently high mobility to ensure the fast variation of the space charge proportionally to the applied voltage. Then, as a first step, we propose to add an electron source term in each point of the computational domain to modify the space charges when the voltage varies to ensure the condition of equation (4) without solving consistently all the drift-diffusion fluxes of charged species in equations (1). This simple approach is non-conservative as we take into account an additional electron source term, but it is important to note that the lack or excess of electrons in the thin non-neutral regions during the spark regime is small compared to the total electron density which increases by orders of magnitude during the spark phase.

In this work, the transition between the streamer model presented in section 2.1 and the spark model presented in this

section is carried out when two conditions are fulfilled: (1) the axial electron density is ten times higher than in the positive streamer channel before connection (i.e. at  $T_g = 1000$  K, the transition is for an electron density higher than  $10^{14} \text{ cm}^{-3}$ ) and (2) the axial electric field is uniform and equal within 10% to the average electric field (i.e. the applied voltage by the gap length). After the transition to the spark model, this model is used until the end of the discharge pulse. The transition between both models usually occurs 0.5 ns after the connection of both streamer discharges. During the spark phase, the model time-step is calculated as  $\delta t = \min(10^{-10}, A_S \delta t_S)$  where  $A_S$  and  $\delta t_S$  are defined in section 2.1. As in the streamer phase in section 2.1, the upper limit value of  $10^{-10}$  s is used as a characteristic time-step to follow accurately the time evolution of the nanosecond applied voltage.

## 2.3. Model for the hydrodynamic expansion after the voltage pulse

To study the coupling of fast-heating nanosecond pulsed discharges with ambient air, we have to question the necessity to solve the neutral gas flow equations during the voltage pulse. If the temperature increase during the voltage pulse is very small ( $< 10$  K), the neutral gas density remains constant and then, there is no need to solve flow equations during the voltage pulse. If the temperature increase during the voltage pulse is more significant, the gas density may vary during the voltage pulse and then change the reduced electric field. In this case, the gas heating has a significant influence on the discharge dynamics. We have then compared the duration of the pulse  $T_{\text{pulse}}$  with the characteristic time for the change of neutral gas density due to heating, defined as  $R_s/c_{\text{max}}$  where  $R_s$  is the typical radius of the discharge, and  $c_{\text{max}}$  is the maximum of the speed of sound in the path of the discharge. The increase of the neutral gas temperature leads to an increase of the speed of sound:  $c_{\text{max}} \propto \sqrt{T_{g,\text{max}}}$ . Then, the time necessary for acoustic waves to propagate inside the heated region is a good approximation of the time-scale of the neutral gas density variation. It is interesting to note that if

$$T_{\text{pulse}} \ll \frac{R_s}{c_{\text{max}}} \quad (5)$$

neutral species are immobile during the voltage pulse. Then even if the temperature increases during the voltage pulse, the neutral gas density remains the same (Naidis 2008). In this case, the temperature increase has an influence on transport coefficients and rate coefficients in source terms but its impact on the discharge dynamics is small. It is important to note that the condition given by equation (5) is rather strict as the temperature field generated by the discharge is highly non-uniform. For an intense spark discharge condition with a temperature increase up to 3000 K and a discharge diameter of  $500 \mu\text{m}$ , the condition given by equation (5) becomes  $T_{\text{pulse}} \ll 500$  ns. As in our case, the durations of voltage pulses are in the range of 5 to 10 ns, the condition given by equation (5) is fulfilled. Then in our conditions, there is no need to solve the flow equations during the voltage pulse and we have used the approximation of a constant neutral gas density during the voltage pulse.

As mentioned in the introduction, in recent years, several works (Popov 2001, Naidis 2008, Aleksandrov 2010, Popov 2011a, 2011b, Mintousov *et al* 2011, Rusterholtz *et al* 2012, Rusterholtz 2012) have been devoted to the study of the fast relaxation of the energy stored in the different internal modes of molecules and atoms in air and the subsequent rapid increase of the translational temperature of the neutral gas. However, there are still some uncertainties on the chemical processes involved and the reaction rate coefficients of some reactions involving excited states. Therefore, as a first step, in this work, we have carried out a parametric study and assumed that a fraction  $\eta_R$  of the discharge energy goes to fast heating. For the conditions of the nanosecond spark discharge studied in this work, based on Popov (2011a) and Aleksandrov (2010), we have considered as a reference in sections 3.1 and 3.4 that  $\eta_R = 30\%$  of the discharge energy instantaneously heats the ambient air. Then, to discuss the influence of  $\eta_R$  on the results, in section 3.2 we consider two other values of  $\eta_R = 15\%$  and  $60\%$ . Finally, we have assumed in section 3.3 that the heating of the neutral gas by the discharge (with  $\eta_R = 30\%$ ) occurs during a characteristic relaxation time  $\tau_h$  after the voltage pulse.

First, if the discharge instantaneously heats the neutral gas during the voltage pulse, at each point of the computational domain during the integration time-step  $dt$  we have:

$$\int_t^{t+dt} c_v dT_g(t) = \frac{\eta_R}{\rho_0} (e_J(t+dt) - e_J(t)) \quad (6)$$

where  $c_v$  is the specific thermal capacity of air at constant volume and  $\rho_0$  is the density of the neutral gas which is assumed to be constant during the voltage pulse. Equation (6) is solved to derive  $T_g(t)$  assuming that  $c_v$  is constant and using a predictor–corrector method. As an instantaneous gas heating is assumed, the maximal air temperature is obtained at the end of the voltage pulse. This temperature field is used as initial condition for the 2D neutral gas flow equations. In the following, to avoid confusion, we use time  $t_l$  which starts at the beginning of the voltage pulse to present results on the nanosecond discharge and time  $t = t_l - T_{\text{pulse}}$  to present flow results after the voltage pulse. In this work, as we study the hydrodynamic expansion on short time scales ( $t \leq 10 \mu\text{s}$ ) after a nanosecond spark discharge to compare with experimental results (Xu *et al* 2011), as a first step, we have neglected viscous and diffusive terms. Then we consider 2D axisymmetric Euler equations:

$$\begin{cases} \partial_t \rho + \nabla \cdot (\rho \mathbf{V}) = 0 \\ \partial_t (\rho V_x) + \nabla \cdot (\rho V_x \mathbf{V}) = -\partial_x p \\ \partial_t (\rho V_r) + \nabla \cdot (\rho V_r \mathbf{V}) = -\partial_r p \\ \partial_t (\rho u_t) + \nabla \cdot (\rho h_t \mathbf{V}) = S_{\text{ener}} \end{cases} \quad (7)$$

$$\text{with} \quad u_t = \frac{1}{2} V^2 + u, \quad u = c_v T_g = \frac{R_s T_g}{(\gamma - 1)}$$

$$\text{and} \quad h_t = u_t + \frac{p}{\rho},$$

where  $\rho$  is the density of the neutral gas,  $V_x$  and  $V_r$  are, respectively, the axial and the radial components of the fluid velocity  $\mathbf{V}$ ,  $u_t$  is the specific total energy of the neutral gas, defined as the sum of the specific kinetic energy and of the

specific internal energy  $u$ ,  $h_t$  is the specific total enthalpy,  $R_s$  is the specific gas constant,  $\gamma$  is the isentropic coefficient of the neutral gas, assumed to be constant and equal to 1.4 and  $S_{\text{ener}}$  is an energy source term which is equal to zero in the case of an instantaneous gas heating. The system given by equations (7) is closed by the ideal gas state equation:

$$p = \rho u (\gamma - 1). \quad (8)$$

Second, we have assumed that the heating of the neutral gas by the discharge occurs at a finite rate after the voltage pulse. More precisely, we have considered a negligible gas heating during the voltage pulse and we have assumed that a fraction of the discharge energy at the end of the voltage pulse  $\eta_R e_J(T_{\text{pulse}})$  is put into the air heating with a characteristic time of  $\tau_h \gg T_{\text{pulse}}$ . Then as initial condition of the Euler simulations, we have considered ambient air at a given and uniform temperature  $T_g$  and we have solved Euler equations (equations (7)) with the energy source term given by:

$$\begin{cases} S_{\text{ener}} = \frac{\eta_R e_J(T_{\text{pulse}})}{\tau_h} (t - T_{\text{pulse}}) & \text{for } T_{\text{pulse}} \leq t \leq \tau_h \\ S_{\text{ener}} = 0 & \text{for } t > \tau_h. \end{cases} \quad (9)$$

For both gas heating models, the governing 2D Euler equations (equations (7)) are solved for a cylindrical geometry using a finite volume approach. The third-order classical MUSCL scheme proposed by van Leer (1979) is used for fluxes with a Lax–Friedrichs Riemann solver (Shu 1997) and a Minmod slope limiter. A second order Runge–Kutta method is used for time integration. The time-step of integration for the explicit Euler simulations is calculated as  $\delta t = 0.5 \delta t_{\text{CFL}}$  where  $\delta t_{\text{CFL}}$  is the classical Courant–Friedrich–Levy (CFL) time-step. We have checked that with this choice, the temperature increase is less than 10 K during one time-step. Validation test-cases of the 2D axisymmetric Euler code and discussion on the choice of the numerical scheme can be found in Tholin (2012).

The electrode surfaces are considered as reflecting surfaces for the flow. Conversely, to avoid any reflection on the outer boundary of the computational domain during the Euler simulations, we have considered a large computational domain of  $[-39 \text{ cm} : 40 \text{ cm}]$  in the axial direction and  $[0 \text{ cm} : 40 \text{ cm}]$  in the radial direction. A refined and uniform mesh of  $10 \mu\text{m}$  on  $1 \text{ cm} \times 1 \text{ cm}$  centred on the discharge gap is used and then the mesh is expanded in both directions following a geometric progression up to the outer boundaries. It is important to note that the computational domain and the mesh of the Euler simulations are larger and less refined, respectively, than those used for the discharge simulations. Then at the end of the voltage pulse, the gas temperature and the discharge energy calculated from the discharge code are interpolated linearly on the mesh used to compute the Euler equations.

### 3. Results and discussion

#### 3.1. Simulation of the flow expansion following a nanosecond spark discharge at $T_g = 1000 \text{ K}$ : reference test-case

As a reference test-case for nanosecond spark discharge in air at  $T_g = 1000 \text{ K}$ , we consider a point-to-point discharge with

a gap size of 2.5 mm, electrodes with a radius of curvature of  $300\ \mu\text{m}$  and an applied voltage of 5100 V. This test-case is very close to the multi-pulse spark discharge studied experimentally in Rusterholtz *et al* (2012). Figure 1 shows the shape of the voltage pulse with rise and decrease times of 2 ns, and a pulse duration of 10 ns and the conductive current calculated using equation (2) for a surface  $S$  located close to the cathode at  $x = 0.75\ \text{cm}$ . Figure 2 shows the distributions of the absolute value of the electric field, the electron density and the discharge energy at  $t_i = 4, 6, 8$  and 10 ns. The gas temperature distributions during the voltage pulse are also shown, assuming that  $\eta_R = 30\%$  of the discharge energy heats instantaneously the ambient air at  $T_g = 1000\ \text{K}$ . In this test-case, the connection between positive and negative discharges occurs at  $t_i = 4.5\ \text{ns}$ . During the streamer phase for  $t_i \leq 4.5\ \text{ns}$ , figure 1 shows that the conductive current calculated for a surface  $S$  located close to the cathode at  $x = 0.75\ \text{cm}$  is very small. During the streamer phase, the conductive current depends of the location of the  $S$  surface in equation (2). However, whatever the location of the  $S$  surface, we have checked that the calculated conductive current remains very small, in agreement with the conductive current obtained in experiments (Rusterholtz *et al* 2012). For  $t_i \geq 4.5\ \text{ns}$ , the discharge transits rapidly to a spark phase with a fast increase of the conductive current and of the energy density. It is interesting to note that during the spark phase, the conductive current is independent of the location of the  $S$  surface in equation (2). In figure 1, we observe a peak of conductive current at about  $t_i = 8\ \text{ns}$  of 40 A, in agreement with the current obtained in experiments (Rusterholtz *et al* 2012) and then the current decreases due to the decrease of the applied voltage. Figure 2 shows that the energy density distribution is non-uniform in the interelectrode gap during the voltage pulse with peaks close to both electrodes. Indeed, as the discharge radius is smaller close to point electrodes than in the middle of the gap, the conductive current and then the discharge energy are higher close to electrodes. Figure 2 also shows that the air temperature increases rapidly during the spark phase. At the end of the voltage pulse at  $t_i = T_{\text{pulse}} = 10\ \text{ns}$ , we observe a hot channel on the discharge path with two hot spots close to electrodes. As we have assumed an instantaneous heating of ambient air by the nanosecond discharge, the air temperature  $T_g(t_i = T_{\text{pulse}})$  obtained at the end of the voltage pulse is used as initial condition for the gas-dynamic Euler equations (i.e.  $t = t_i - T_{\text{pulse}} = 0$ ).

The gas density is assumed to be constant during the voltage pulse, then the pressure at the end of the voltage pulse is computed using the ideal gas law considering a density of  $0.35\ \text{kg cm}^{-3}$  for air at 1000 K. Figure 3 shows the 2D distributions of gas temperature, air density, pressure and magnitude of the flow velocity at the end of the voltage pulse and then at the beginning of the Euler simulation. Figure 3 shows that the initial condition consists of an homogeneous gas density in the whole computational domain, and a channel on the discharge path with higher pressure and temperature than ambient air with two hot spots close to electrode tips. Figure 4 shows the 2D distributions of gas temperature, air density, pressure and magnitude of the flow velocity at  $t = 400, 800\ \text{ns}$  and  $1.2\ \mu\text{s}$ . At  $t = 400\ \text{ns}$ , figure 4 shows that the gas

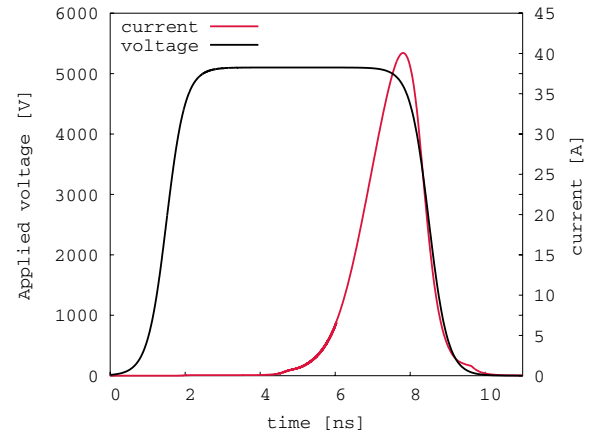


**Figure 1.** Time evolution of the applied voltage and of the conductive current calculated using equation (2) for a surface  $S$  located close to the cathode at  $x = 0.75\ \text{cm}$  for the reference spark discharge in air at  $T_g = 1000\ \text{K}$  for a point-to-point configuration with a gap size of 2.5 mm and electrodes with a radius of curvature of  $300\ \mu\text{m}$ , close to the conditions studied experimentally in Rusterholtz *et al* (2012).

density has significantly decreased in the discharge channel and particularly close to the electrode tips. We also note that the velocity of the fluid has a cylindrical shape all around the heated channel with a slightly higher value close to the hot spots. For  $t > 400\ \text{ns}$ , a cylindrical shock wave characterized by jumps in pressure, density, temperature and velocity propagates radially. These jumps are more significant in the region close to the electrode tips due to a higher initial temperature. However, the shock wave propagation velocity is at every point of the wave front equal to the speed of sound in the unperturbed air at 1000 K ( $650\ \text{m s}^{-1}$ ) as observed in experiments (Xu *et al* 2011). Behind the shock wave, a low density region is formed with a pressure less than the atmospheric pressure. This depletion is a consequence of the air displacement due to the velocity induced by the shock wave. It can be interpreted as the fast dilatation of the hot channel produced by the discharge. Between  $t = 800\ \text{ns}$  and  $1.2\ \mu\text{s}$  two other shock waves propagate from the electrode tips in the low pressure, low density channel. These shock waves are reflections of the first cylindrical shock wave on the electrode tips. These successive shock waves increase the gas density in the hot channel and the pressure slowly converges to the atmospheric pressure for  $t > 1.2\ \mu\text{s}$ . Figure 5 shows that at  $t = 10\ \mu\text{s}$ , a hot channel with a low density is formed on the discharge path with a uniform atmospheric pressure. We point out that the temperature in the hot channel at  $t = 10\ \mu\text{s}$  is less than the initial one in figure 3, as the shock wave propagation has removed part of the initial hot channel energy.

Figure 6 shows the time evolution of the air density and temperature in the radial direction in the middle of the inter-electrode gap every 100 ns up to 900 ns. In the first 600 ns, we note a fast depletion of the air density and of the gas temperature inside the hot channel. On the density profiles, we note that the shock wave is formed on the wings of the heated channel before propagating radially towards the surrounding ambient air. Due to the cylindrical symmetry, the amplitude of the shock wave decreases as it propagates radially. The



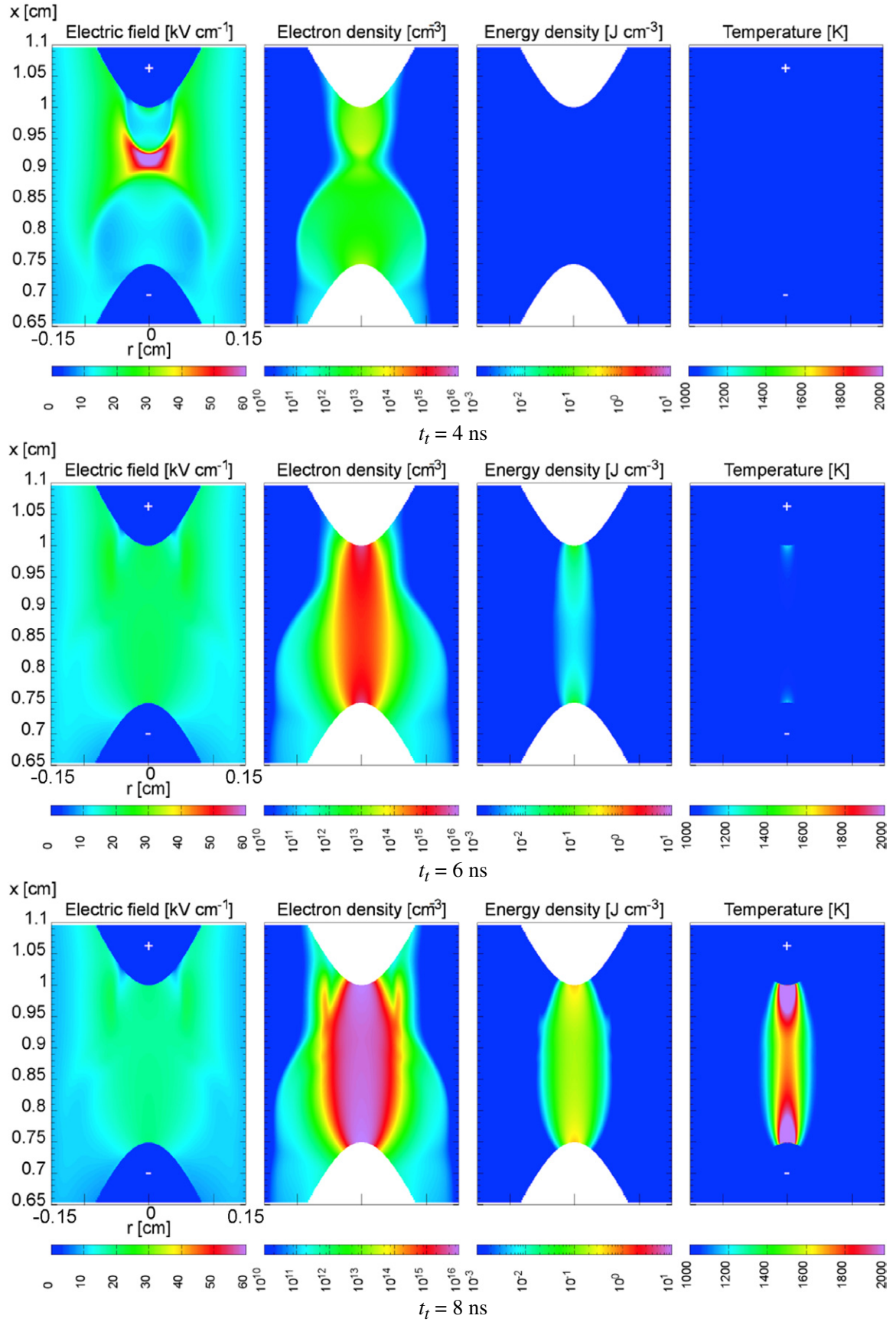


**Figure 2.** Cross-sectional views of the magnitude of the electric field, electron density, discharge energy density and neutral gas temperature for the reference nanosecond spark of figure 1 in air at  $T_g = 1000$  K. The neutral gas temperature is obtained assuming an instantaneous gas heating with  $\eta_R = 30\%$  (see section 2.3).



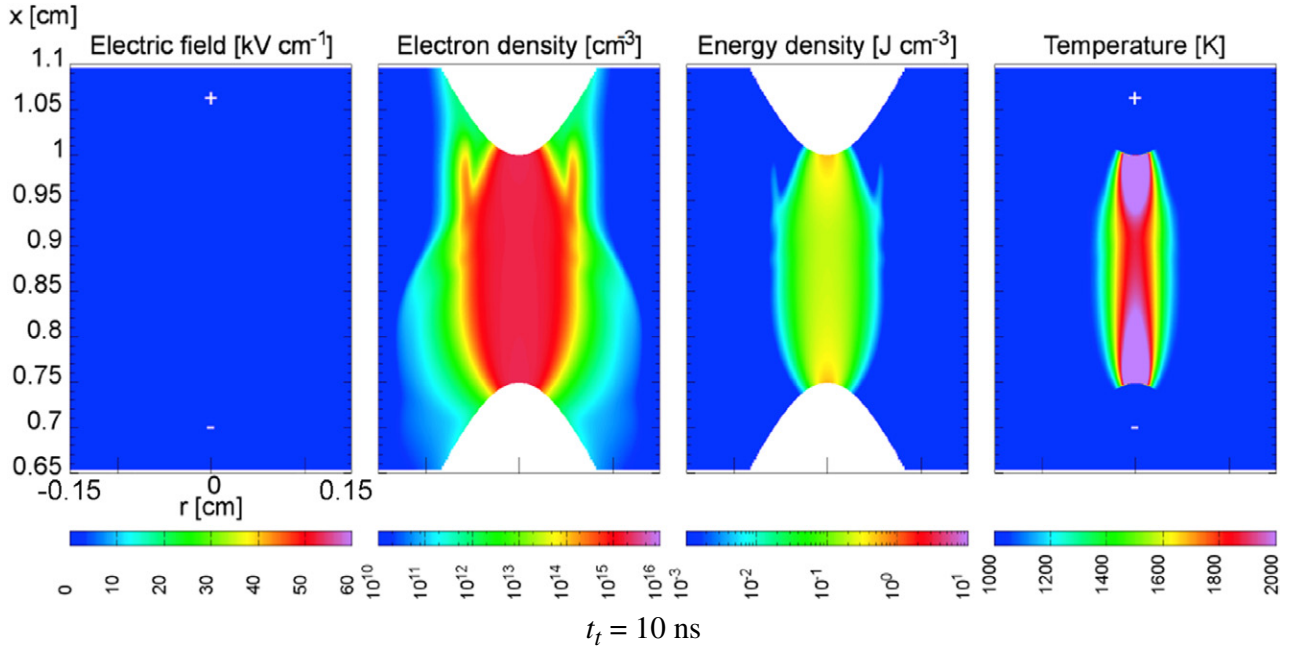
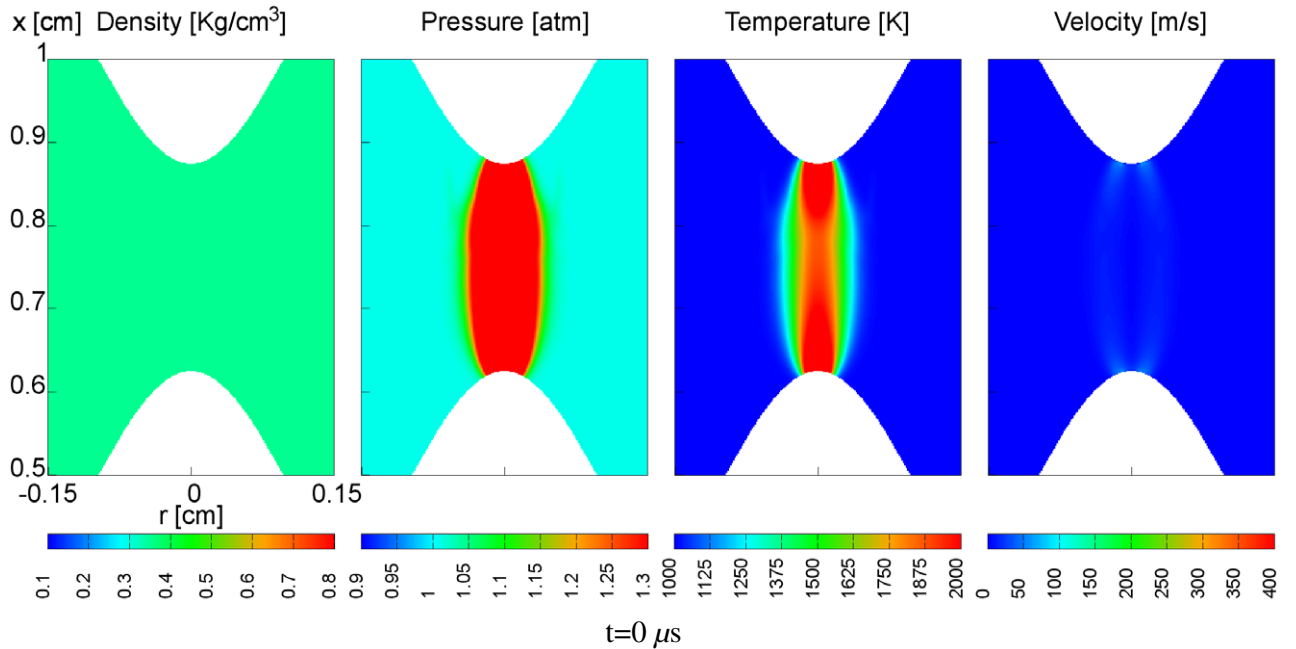


Figure 2. (Continued).



**Figure 3.** Cross-sectional views of the density, pressure, air temperature and magnitude of the flow velocity at the end of the voltage pulse for the reference nanosecond spark discharge of figure 1 in air at  $T_g = 1000$  K assuming an instantaneous gas heating with  $\eta_R = 30\%$  (see section 2.3). This corresponds to the initial condition for the 2D Euler simulations.

maximum density inside the shock wave is around  $0.4 \text{ kg cm}^{-3}$  which corresponds to an increase of 15% in comparison of the density of  $0.35 \text{ kg cm}^{-3}$  of the surrounding ambient air at  $T_g = 1000$  K. The maximum temperature jump behind the shock wave in the radial direction in the middle of the gap in figure 6 is around 40 K. Figure 4 shows that the temperature field is non-uniform axially and higher temperature jumps up to 200 K are obtained close to the electrodes. The maximum temperature jump due to the shock wave is then of about 20%, but as the shock wave propagates this temperature

jump decreases and becomes very small. As a consequence, as the speed of sound is proportional to the square root of the air temperature, the speed of sound of the steady air is barely affected by the presence of the shock wave. Then, the generated shock waves propagate at velocities very close to the speed of sound at  $T_g = 1000$  K. Figure 6 also shows that the hot channel increases in size as a function of time for  $t \leq 1 \mu\text{s}$ . If we define the radius of the hot channel as the distance from the axis of symmetry at which the density is equal to the density of the ambient air (in our case  $0.35 \text{ kg cm}^{-3}$ ), our

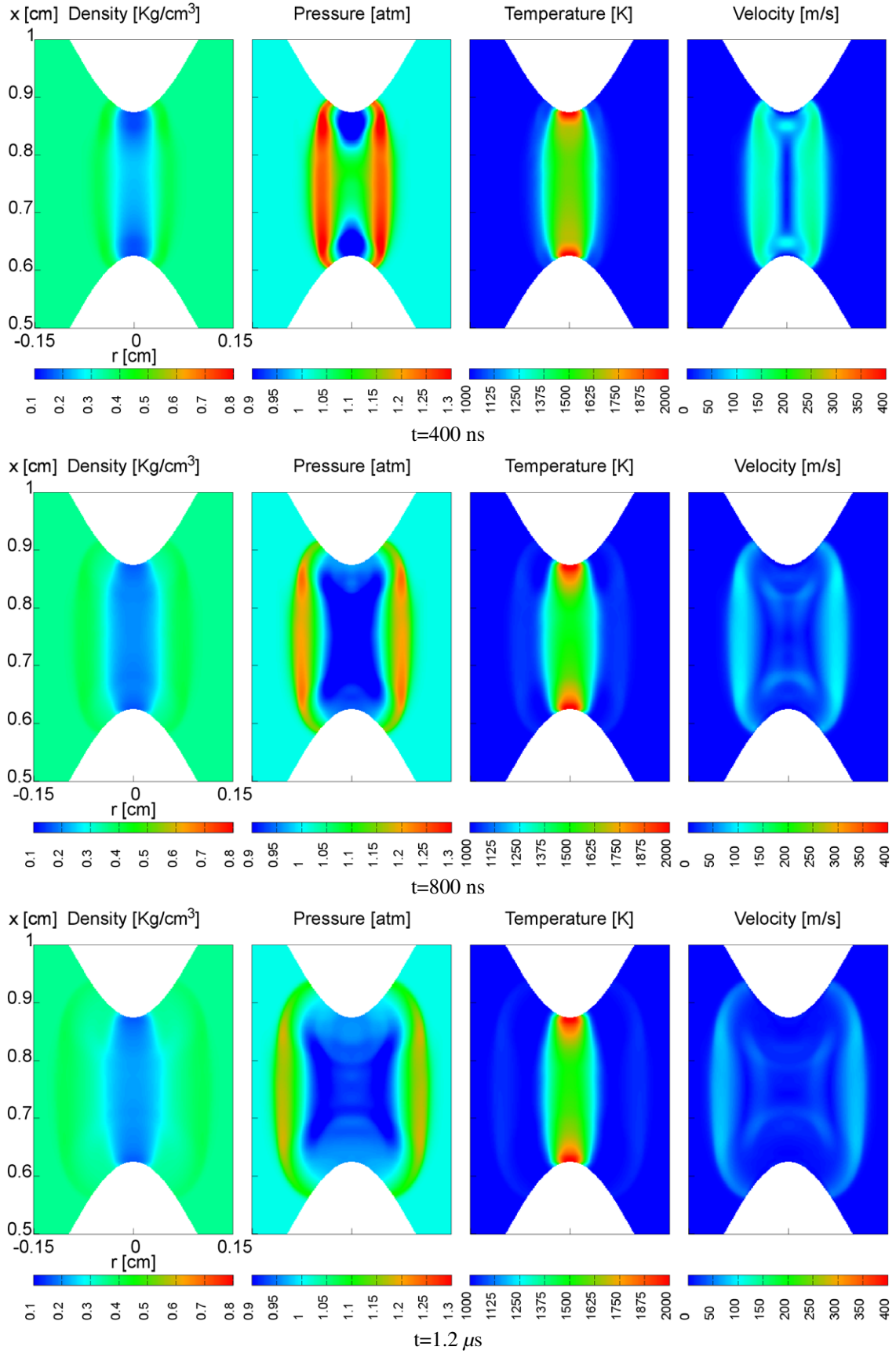


**Figure 4.** Cross-sectional views of density, pressure, air temperature and magnitude of flow velocity for  $t = 400, 800$  and  $1.2$   $\mu$ s for the initial condition of figure 3 in air at  $T_{\text{g}} = 1000$  K.

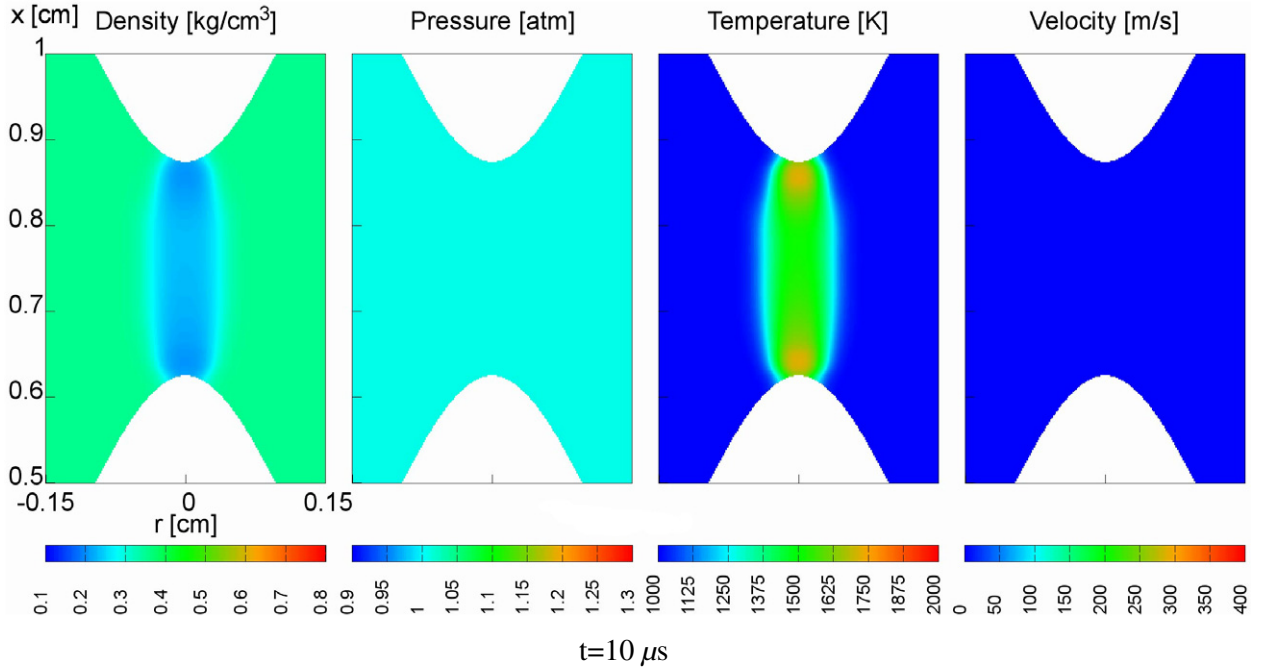


**Figure 5.** Cross-sectional views of the density, pressure, air temperature and magnitude of the flow velocity at  $t = 10 \mu\text{s}$  for the initial condition of figure 3 in air at  $T_g = 1000 \text{ K}$ .

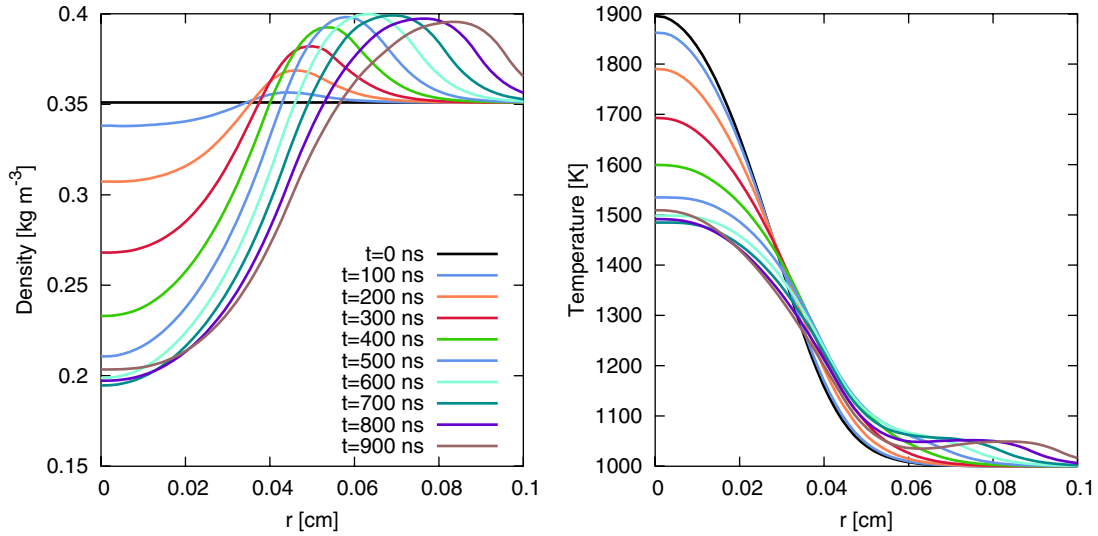


**Figure 6.** Time evolutions of the air density and the air temperature in the radial direction in the middle of the gap every 100 ns up to 900 ns for the same condition as figure 4.

results show that this radius increases between 300 and 900 ns by 60%. The expansion velocity of the heated channel for  $t \leq 1 \mu\text{s}$  is around  $660 \text{ m s}^{-1}$  which is a little higher than the speed of sound at  $T_g = 1000 \text{ K}$ . It is interesting to point out that this fast expansion of the heated channel on short time-scales is also observed in experiments (Xu *et al* 2011). Figure 7 shows the time evolution of the air density and the temperature in the axial direction on the symmetry axis every 100 ns up to 900 ns. The initial temperature distribution is non-uniform on the discharge axis with a 1000 K difference between the temperature at electrode tips and in the middle of the gap. Figure 7 shows that the air density and temperature decreases are more significant close to the electrode tips than

in the middle of the gap: in the first 400 ns, the temperature decrease is around 400 K in the middle of the gap and around 1000 K at the tip of the electrodes. This faster decrease of temperature close to electrodes is due to the higher pressure and the faster shock wave formation, which is able to remove a significant amount of the deposited energy. However, for  $t > 600 \text{ ns}$ , the temperature difference between the electrode tips and the middle of the gap remains rather constant and equal to about 600 K. As a consequence, the 2D temperature distribution in the hot channel obtained in figure 5 for  $t = 10 \mu\text{s}$  is more homogeneous than at the end of the voltage pulse (figure 3). Finally, it is interesting to note that the different succeeding shock waves have removed a significant amount

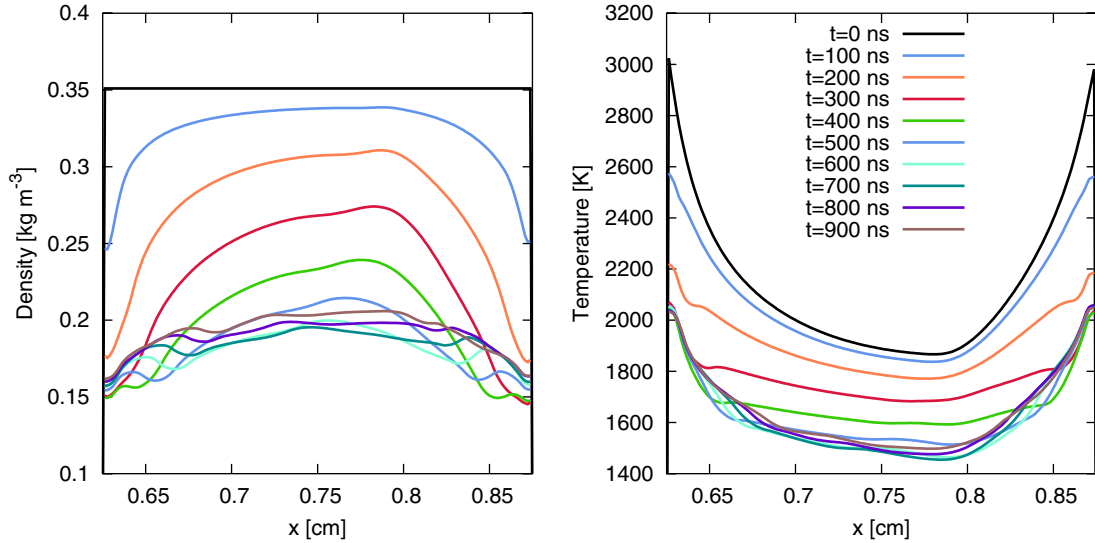


**Figure 7.** Time evolutions of the air density and the air temperature in the axial direction on the symmetry axis every 100 ns up to 900 ns for the same condition as figure 4.

of the discharge energy deposited in the gas: the temperature decrease after the shock wave propagations is around 30% at the tip of the electrodes and 20% in the middle of the gap.

Then the good agreement obtained with experiments in Xu *et al* (2011) on the flow expansion after the nanosecond pulsed spark discharge, validates *a posteriori* the simple spark model presented in section 2.2 and seems to confirm that the gas heating by the nanosecond spark discharge in Xu *et al* (2011) is very fast.

### 3.2. Influence of the fraction of discharge energy going to fast gas heating on the flow expansion following a nanosecond spark discharge at $T_g = 1000$ K

In the previous section, we have assumed that  $\eta_R = 30\%$  of the total discharge energy instantaneously heats the ambient air. In this section, we have considered two other values of  $\eta_R = 15\%$  and  $60\%$  to study its influence on the gas dynamics. Figure 8 shows the time evolutions of the air density and air temperature in the radial direction in the middle of the inter electrode gap every 100 ns up to 900 ns for  $\eta_R = 15\%$  and  $\eta_R = 60\%$ . Figure 9 shows for the same conditions, the time evolutions of the air density and the temperature in the axial direction on the symmetry axis. First, it is interesting to note that for the different studied values of  $\eta_R$  in the range 15% to 60%, we observe very similar shock wave structures and a very similar dynamics of the flow. In all cases, the propagation velocity of shock waves is very close to the speed of sound in steady air at 1000 K. As expected, as the value of  $\eta_R$  increases, more energy is put into the ambient air and the generated shock wave induces higher density, pressure, and temperature gradients. For example, at  $t = 0$  ns the temperature increase is about four times higher on the axis in the middle of the gap for  $\eta_R = 60\%$  than for  $\eta_R = 15\%$ . Correspondingly, the air density decrease in the first 600 ns on the axis in the middle of the gap is two times higher for  $\eta_R = 60\%$  than for  $\eta_R = 15\%$ . In figure 8, we also note that the shock wave generated by the low density channel propagates slightly faster at the beginning

of its propagation for  $\eta_R = 60\%$  than for  $\eta_R = 15\%$ . On the radial profiles of the air density, we observe that between 100 and 900 ns, the radius of the hot channel increases by 50% for  $\eta_R = 15\%$ . For  $\eta_R = 60\%$ , the radius of the hot channel increases by 67% in the same time, corresponding to a much faster and more significant dilatation of the hot channel. It is interesting to note that the rapid dilatation of the hot channel for  $t \leq 1 \mu\text{s}$  has been obtained for all values of  $\eta_R$  studied in this work in assuming an instantaneous heating of ambient air. As this fast expansion of the hot channel is also observed in experiments (Xu *et al* 2011) at  $T_g = 1000$  K, the results obtained in section 3.1 and in this section seem to confirm the very fast heating of the ambient air by the nanosecond spark discharge in Xu *et al* (2011). However, additional more quantitative experimental studies are required to derive the value of  $\eta_R$  from the comparison of experimental results in Xu *et al* (2011) and numerical results.

### 3.3. Influence of the gas heating relaxation time on the flow expansion following a nanosecond spark discharge at $T_g = 1000$ K

In previous sections, we have assumed that the fraction  $\eta_R$  of the total discharge energy instantaneously heats the ambient air. However, the air heating by the nanosecond discharge is due to the relaxation of the energy stored in different internal modes of molecules and atoms, which may have very different timescales. The hypothesis of an infinitely fast-heating rate is valid only if the fast-heating process occurs in a characteristic time which is much less than the diameter of the discharge divided by the speed of sound in the hot channel, which is around 500 ns for a strong spark discharge (see section 2.3). In experiments (Rusterholtz *et al* 2012), the characteristic time for the fast gas heating by the nanosecond spark discharge is about 20 ns. As part of preparatory works for the results presented in this work, we have carried out simulations with a 20 ns relaxation time for fast gas heating with  $\eta_R = 30\%$  and no significant differences have been observed on the



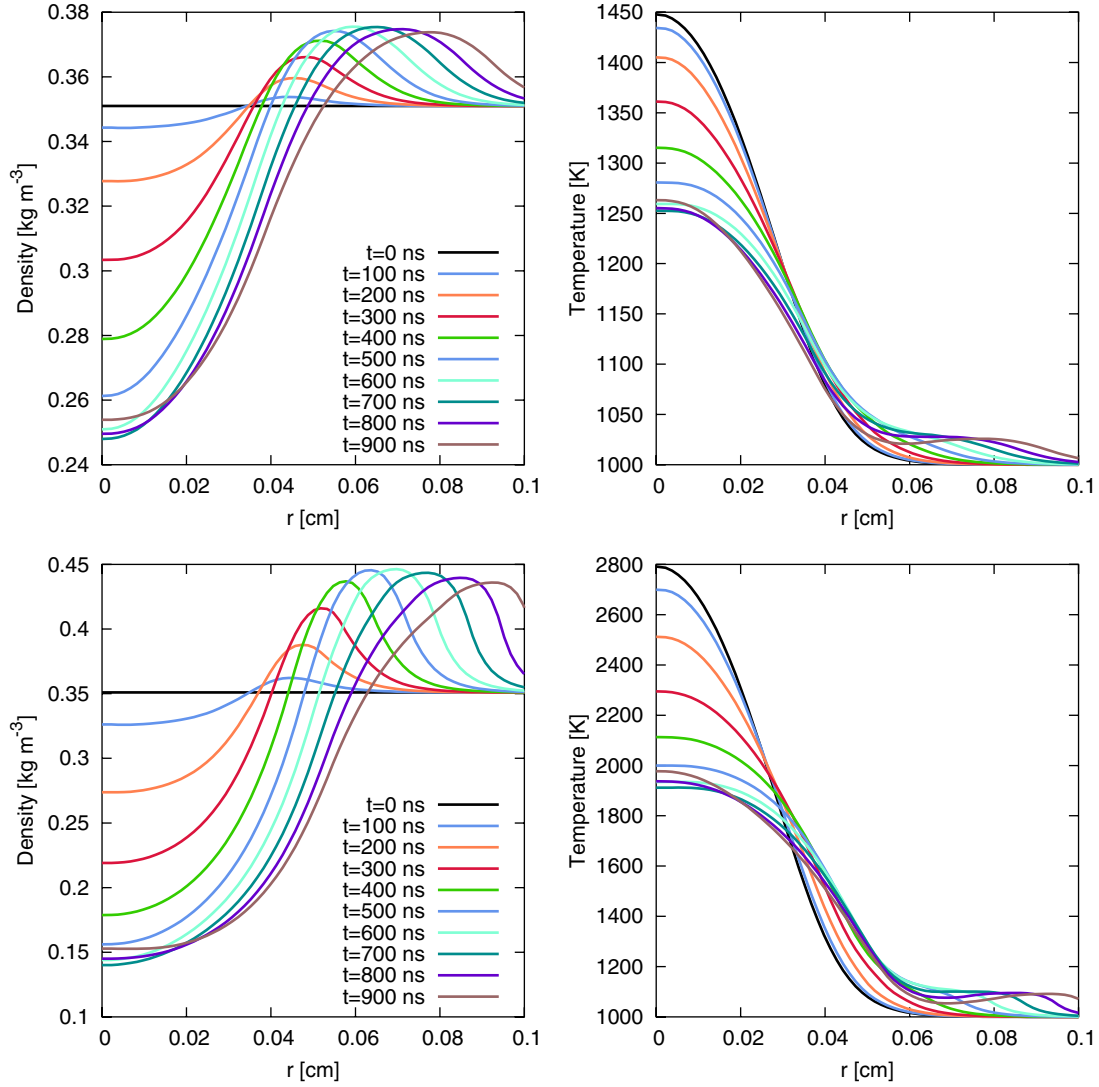


**Figure 8.** Time evolutions of the air density and the air temperature in the radial direction in the middle of the gap every 100 ns after the reference nanosecond spark discharge of figure 2 at  $T_g = 1000$  K assuming an instantaneous gas heating with  $\eta_R = 15\%$  (top figures) and  $\eta_R = 60\%$  (bottom figures).

gas dynamics with the reference case of an infinitely fast gas heating (section 3.1). In this section, we consider no gas heating during the voltage pulse and we assume that a fraction of the discharge energy at the end of the voltage pulse  $\eta_R e_I(T_{\text{pulse}})$  is put into the air heating with a characteristic time of  $\tau_h \gg T_{\text{pulse}}$ . As the upper limit value of  $\tau_h$  for the nanosecond spark discharge studied in this work, in this section we consider  $\tau_h = 1 \mu\text{s}$  as observed in experiments on air surface dielectric barrier discharges at atmospheric pressure (Aleksandrov 2010). Figure 10 shows the time evolutions of the air density and of the temperature in the radial direction in the middle of the gap for  $\eta_R = 30\%$  with  $\tau_h = 1 \mu\text{s}$  up to  $t = 5 \mu\text{s}$ . Figure 11 shows the time evolutions of the air density and of the temperature in the axial direction on the symmetry axis for the same conditions. On both figures, we note that the air temperature at  $t = 0$  s is equal to 1000 K and increases progressively during  $1 \mu\text{s}$ . Conversely, figure 10 shows that the air density decreases progressively and that a pressure wave is generated on the wings of the hot channel and propagates radially towards the ambient air. In figure 10,

we note that the maximum air temperature on the axis in the middle of the interelectrode gap obtained at  $t = 1 \mu\text{s}$  is 100 K less than the maximum initial temperature for the case of an infinitely fast heating (see figure 6). This is due to the fact that with a relaxation time of  $\tau_h = 1 \mu\text{s}$ , the pressure wave is generated and starts to propagate during the temperature increase, removing some energy from the hot channel during its formation. For  $t > 1 \mu\text{s}$ , the temperature on the axis in the middle of the gap starts to slowly decrease and the air density increases slowly up to  $t = 5 \mu\text{s}$ .

It is interesting to note that there are two major differences between the case of the air heating with a characteristic time  $\tau_h = 1 \mu\text{s}$  and an instantaneous heating: first, due to the slow increase of the air temperature when a characteristic time  $\tau_h = 1 \mu\text{s}$  is considered, the amplitude of the generated pressure wave is smaller and smoother than the one obtained for an instantaneously fast heating. Second, with an instantaneous heating, a rapid expansion of the heated channel is observed for  $t \leq 1 \mu\text{s}$  in figure 6. With an air heating with a relaxation time of  $\tau_h = 1 \mu\text{s}$ , figure 10 shows only a small increase of the

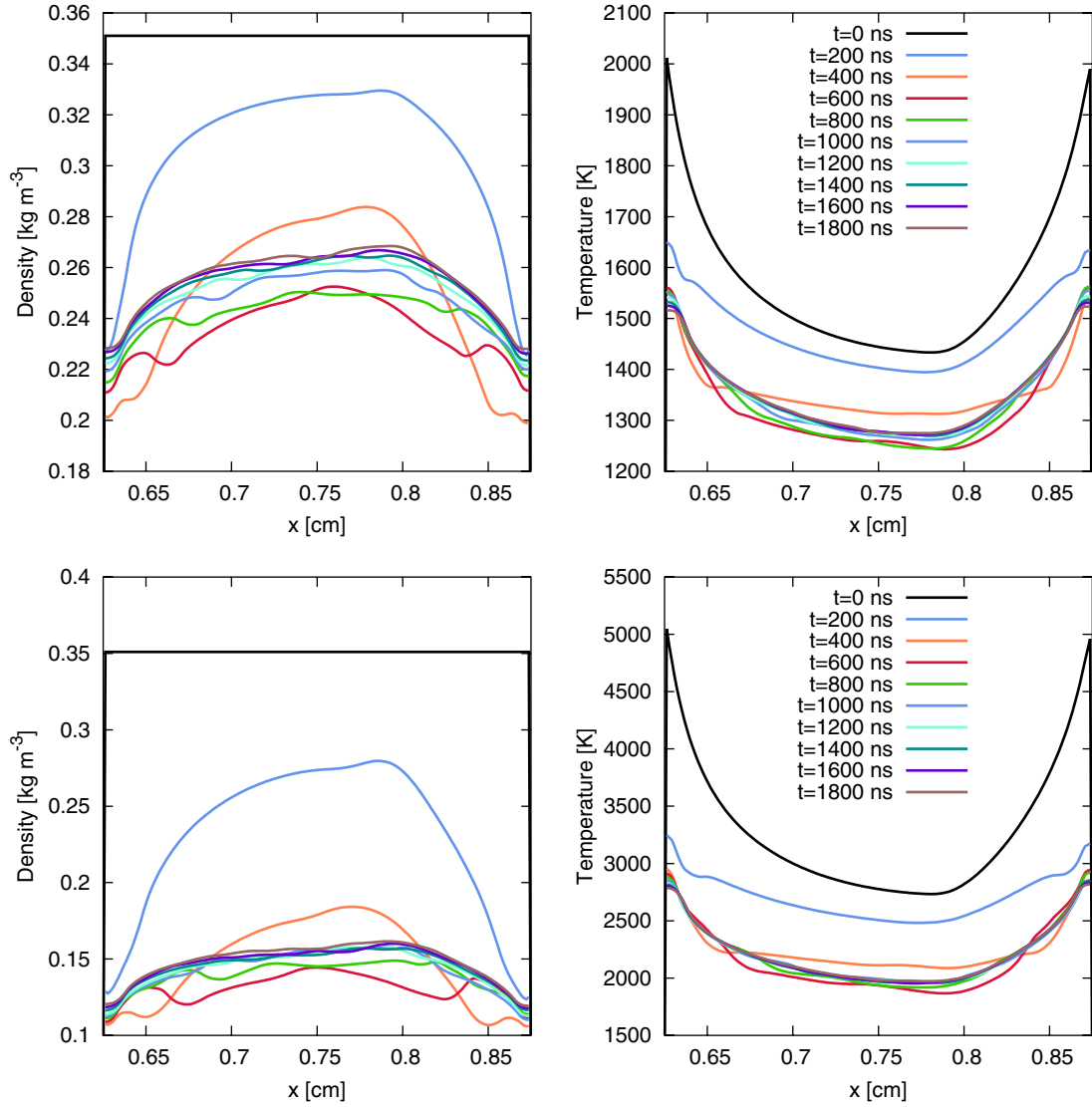


**Figure 9.** Time evolutions of the air density and the air temperature in the axial direction on the symmetry axis every 100 ns after the reference nanosecond spark discharge of figure 2 at  $T_g = 1000$  K assuming an instantaneous gas heating with  $\eta_R = 15\%$  (top figures) and  $\eta_R = 60\%$  (bottom figures).

radius of the hot channel for  $t \leq 1 \mu\text{s}$ . As the fast expansion of the hot channel and the shock wave propagation are clearly observed in the experimental results from Xu *et al* (2011), our simulation results seem to validate the hypothesis of a fast heating on short time-scales much less than  $1 \mu\text{s}$  in the nanosecond spark discharge studied in Xu *et al* (2011).

### 3.4. Simulation of the flow expansion following a nanosecond spark discharge at $T_g = 300$ K

In this section, we consider a nanosecond spark discharge in air at atmospheric pressure at  $T_g = 300$  K. As discussed in Tholin and Bourdon (2011), if we consider a voltage pulse with the same duration and we scale the applied voltage with the air density, the air heating is more significant at  $T_g = 300$  K than at 1000 K. Then after the connection of both streamer discharges, the obtained spark is more intense at  $T_g = 300$  K than at 1000 K. In experiments, the pulsed power-supply limits the current delivered during the spark phase.

Recently, Naidis (2009) has simulated in 1D the significant effect on the power-supply electric circuit on the limitation of the current of pulsed discharges in air at atmospheric pressure. However, the modelling of the electric circuit is beyond the scope of this paper and will be addressed in a future work. Therefore, as a first step, we have considered a configuration in which the voltage pulse decreases only a few nanoseconds after the connection time, to avoid a too intense spark discharge at  $T_g = 300$  K. In this section, we consider the same geometry and initial conditions as for the reference nanosecond spark discharge defined in section 3.1 at  $T_g = 1000$  K but with an applied voltage of 15 kV, scaled relatively to the air density at  $T_g = 300$  K and with a pulse duration of  $T_{\text{pulse}} = 5$  ns (with a rise and a decrease time of 2 ns), shorter than for the reference case at  $T_g = 1000$  K. Figure 12 shows the distributions of the absolute value of the electric field, the electron density and the discharge energy at  $t_i = 3, 4$  and 5 ns. The gas temperature distributions during the voltage pulse are also shown, assuming that  $\eta_R = 30\%$  of the discharge energy heats

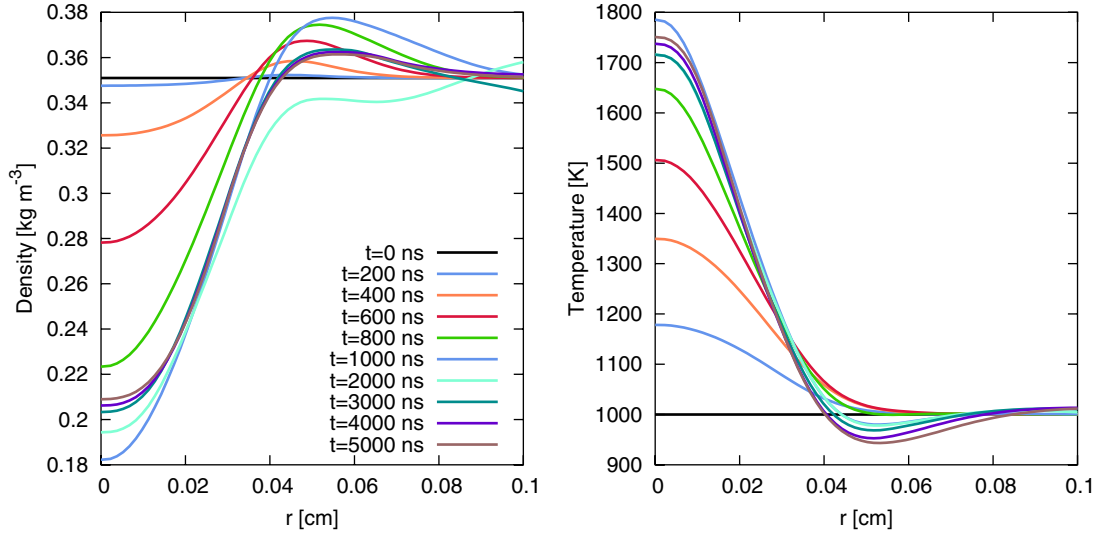


**Figure 10.** Time evolutions of the air density and the air temperature in the radial direction in the middle of the gap up to  $t = 5 \mu\text{s}$  after the reference nanosecond spark discharge of figure 2 at  $T_g = 1000 \text{ K}$  assuming that  $\eta_R = 30\%$  of the discharge energy is put into the air heating with a characteristic time of  $\tau_h = 1 \mu\text{s}$ .

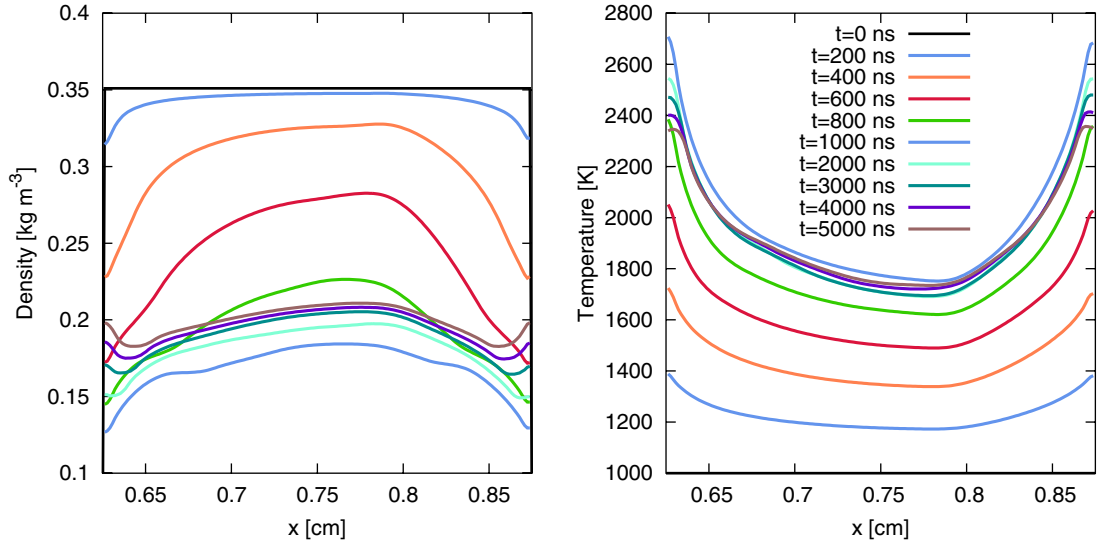


**Figure 11.** Time evolutions of the air density and the air temperature in the axial direction on the symmetry axis up to  $t = 5 \mu\text{s}$  after the reference nanosecond spark discharge of figure 2 at  $T_g = 1000 \text{ K}$  assuming that  $\eta_R = 30\%$  of the discharge energy is put into the air heating with a characteristic time of  $\tau_h = 1 \mu\text{s}$ .

instantaneously the ambient air at  $T_g = 300 \text{ K}$ . In this test-case, the connection between positive and negative discharges occurs at  $t_i = 3.5 \text{ ns}$  and then the discharge transits to a spark phase with a fast increase of energy density and air temperature, but as the voltage pulse lasts only  $5 \text{ ns}$ , the temperature increase is less than the one obtained at  $T_g = 1000 \text{ K}$  (figure 2). Figure 12 shows that the energy density and the air temperature distributions are non-uniform in the interelectrode gap. We point out at  $t_i = 4 \text{ ns}$ , just after the connection, two hot spots close to the electrode tips and a third one in the middle of the gap. At  $T_g = 1000 \text{ K}$  (figure 2), only the two hot spots close to the electrode tips are observed just after the connection. At  $T_g = 300 \text{ K}$ , the third hot spot in the middle of the gap is directly linked to the discharge structure: indeed, in figure 12, we observe at  $t_i = 3$  and  $4 \text{ ns}$  a constriction of the discharge radius in the middle of the gap (which is not seen

in the reference case at  $T_g = 1000 \text{ K}$ ). This constriction of the discharge increases the local current density and then the deposited energy density. At  $t_i = T_{\text{pulse}} = 5 \text{ ns}$ , at the end of the voltage pulse, figure 12 shows that a hot channel is obtained in the discharge path, with a non-uniform axial temperature profile with a hot cylinder from the middle of the gap up to the anode tip and a hot spot close to the cathode tip. This temperature field is used as initial condition for the 2D neutral gas flow equations at  $t = t_i - T_{\text{pulse}} = 0$ . Figure 13 shows the gas dynamics following the nanosecond spark at  $T_g = 300 \text{ K}$ . We observe at  $t = 600 \text{ ns}$  a fast depletion of the air density close to electrode tips and also in the hot region between the anode and the middle of the inter-electrode gap. On the pressure and velocity distributions, we point out that three shock waves emerge at the same time from the three initial hot spots. At  $t = 1.2 \mu\text{s}$  the three spherical shock waves merge into a

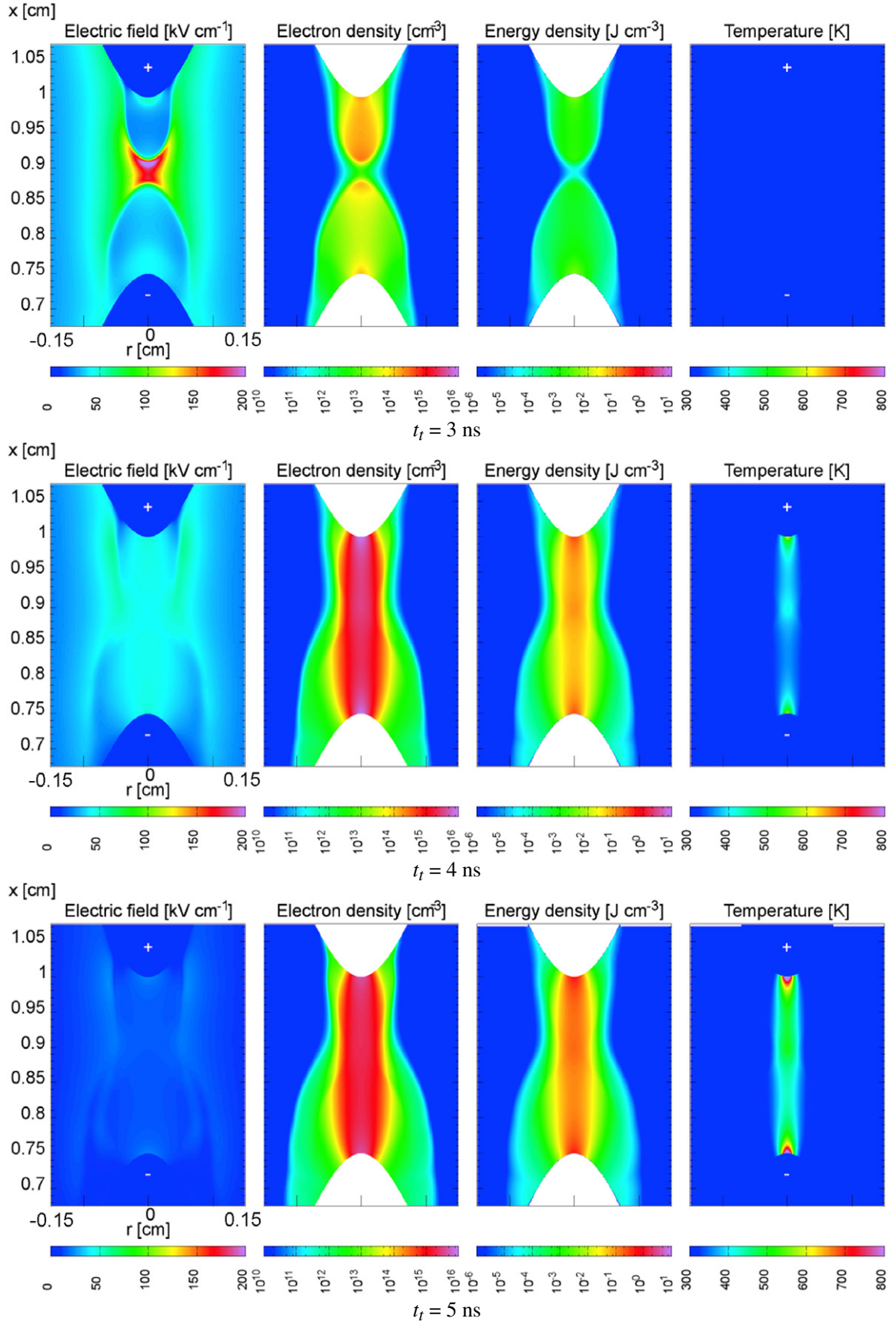


**Figure 12.** Cross-sectional views of the magnitude of the electric field, electron density, discharge energy density and air temperature for a nanosecond spark in air at  $T_g = 300$  K. The air temperature is obtained assuming an instantaneous gas-heating with  $\eta_R = 30\%$  (see section 2.3).



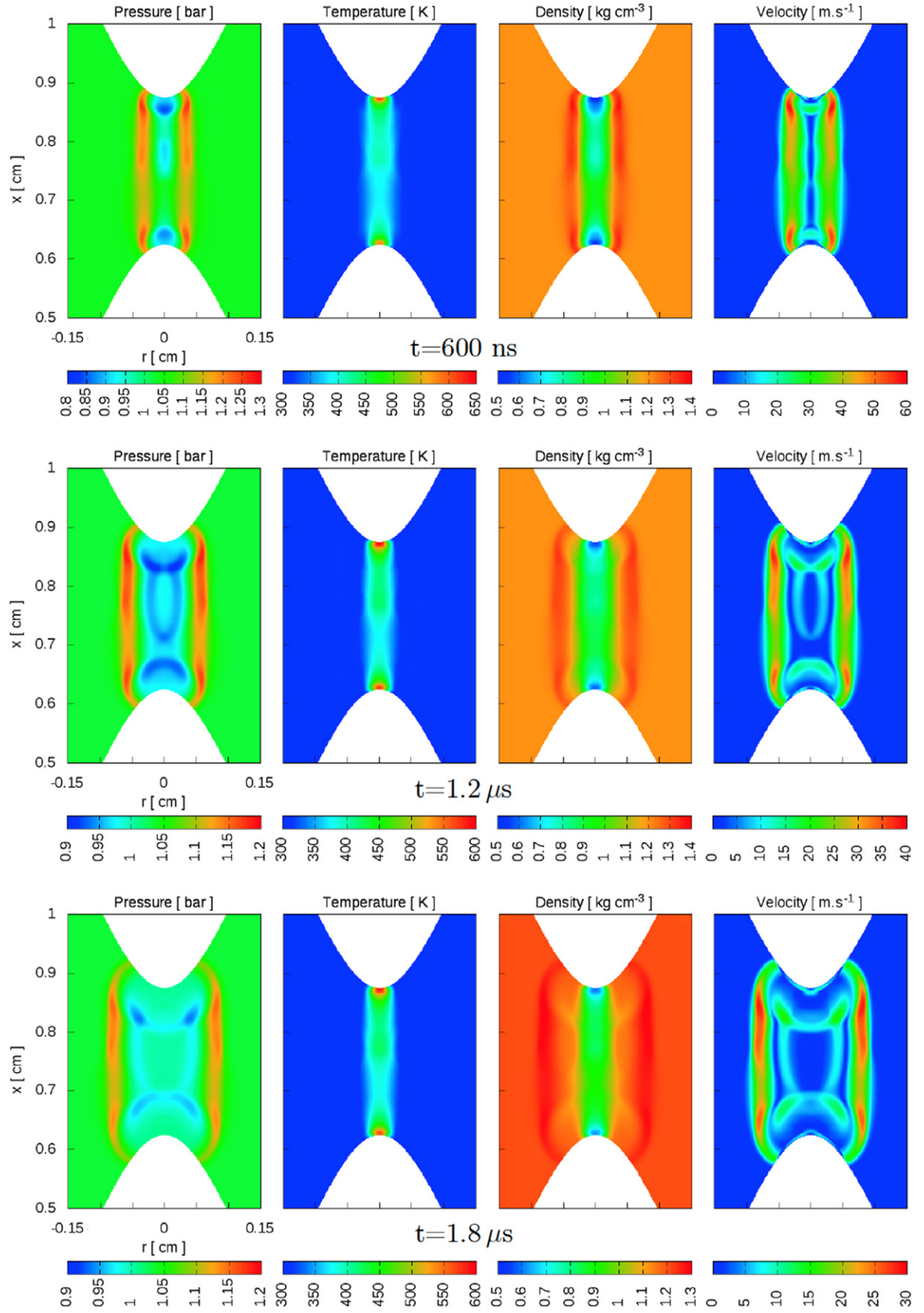


**Figure 13.** Cross-sectional views of density, pressure, air temperature and magnitude of flow velocity for  $t = 600$ ,  $1.2$  and  $1.8 \mu s$  after the nanosecond spark discharge of figure 12 in air at  $T_g = 300$  K.

cylindrical shock wave propagating radially at approximately  $360 \text{ m s}^{-1}$ , i.e. a velocity very close to the speed of sound at  $T_g = 300 \text{ K}$ . These results are in good qualitative agreement with experiments in Xu *et al* (2011) at  $T_g = 300 \text{ K}$ . Finally at  $t = 1.8 \mu\text{s}$ , we observe a hot channel, with a lower temperature and slightly more homogeneous temperature distribution than at  $t = 0 \text{ ns}$  due to the shock wave propagation. For  $t > 1.8 \mu\text{s}$ , we have checked that the pressure converges to the atmospheric pressure and then that we obtain a hot, low density channel on the discharge path, as for the reference spark discharge at  $T_g = 1000 \text{ K}$ . These results are in good qualitative agreement with experiments in Xu *et al* (2011) at  $T_g = 300 \text{ K}$  and seem to confirm the very fast heating of the ambient air by the nanosecond spark discharge in Xu *et al* (2011).

#### 4. Conclusions

The principal results and contributions, which follow from studies presented in this paper on air discharges in point-to-point geometry at atmospheric pressure, can be summarized as follows:

- (i) At  $T_g = 300 \text{ K}$  and  $1000 \text{ K}$ , we have simulated in 2D the formation of a nanosecond spark discharge in air at atmospheric pressure, the induced air heating and the following hydrodynamic expansion. In a first step, we have considered that a fixed fraction  $\eta_R$  of the discharge energy instantaneously heats the ambient air. As a reference, we have used the value of  $\eta_R = 30\%$  based on the works of Popov (2001) and Aleksandrov (2010). At the end of the voltage pulse, we have shown that the energy density and the air temperature distribution are non-uniform in the interelectrode gap with two hot spots close to the electrode tips at  $T_g = 1000 \text{ K}$ . At  $T_g = 300 \text{ K}$ , at the end of the voltage pulse, a hot cylinder is formed from the middle of the gap up to the anode tip and a hot spot is also seen close to the cathode tip. After the nanosecond voltage pulse, we have observed the formation and propagation of a cylindrical shock wave and its reflection on the electrode tips for  $T_g = 300 \text{ K}$  and  $1000 \text{ K}$ . The propagation velocity of the cylindrical shock wave is very close to the speed of sound of air at the studied  $T_g$ . We have also observed the rapid dilatation of the hot channel formed on the discharge path for  $t \leq 1 \mu\text{s}$ . These results are in good qualitative agreement with experiments in Xu *et al* (2011).
- (ii) In a second step, we have carried out a parametric study on the influence of the value of  $\eta_R$  on the air heating and hydrodynamic expansion at  $T_g = 1000 \text{ K}$ , assuming an instantaneously fast gas heating. For all values of  $\eta_R$  studied in this work in the range of 15% to 60%, we have observed the formation and propagation of a cylindrical shock wave with a propagation velocity close to the speed of sound in air at  $T_g = 1000 \text{ K}$ , and the rapid dilatation of the hot channel formed on the discharge path for  $t \leq 1 \mu\text{s}$ . Then we have considered that the nanosecond spark discharge heats the ambient air with a longer relaxation time of  $1 \mu\text{s}$ , and in this case we have

observed the propagation of a weak pressure wave and no dilatation of the hot channel on the discharge path. As the hot channel expansion and a shock wave propagation are clearly observed in the experimental results from Xu *et al* (2011), our simulation results seem to validate the hypothesis of a gas heating by the nanosecond spark discharge on very short time-scales. However, additional more quantitative experimental studies are required to derive the value of  $\eta_R$  from the comparison of numerical results and experimental results in Xu *et al* (2011). Finally, in this work, we have simulated the hydrodynamic expansion on short times ( $t \leq 10 \mu\text{s}$ ) after a single pulse spark discharge at  $T_g = 300$  and  $1000 \text{ K}$  to compare with experimental results in Xu *et al* (2011) and then we have neglected heat transfer in the gas and to the electrodes. Furthermore, in this work, we have assumed that the applied voltage is independent of the discharge current. In a future work, we will model the power-supply electric circuit used in experiments and heat transfer processes to study their influence on the multi-pulse spark discharges and on the air hydrodynamics after several successive voltage pulses.

#### Acknowledgments

The authors thank the Agence Nationale de la Recherche for its support of the PREPA (Grant No ANR-09-BLAN-0043-03) and the PLASMAFLAME (Grant No ANR-11-BS09-025-01) projects and Mr Da Xu, Drs Diane Rusterholtz-Duval, David Pai, Deanna Lacoste and Professor Christophe Laux for helpful discussions on their experimental results on nanosecond spark discharges in air.

#### References

- Aleksandrov N L, Kindysheva S V, Nudnova M M and Starikovskiy A Yu 2010 Mechanism of ultra-fast heating in a non-equilibrium weakly ionized air discharge plasma in high electric fields *J. Phys. D: Appl. Phys.* **43** 255201
- Bastien F and Marode E 1985 Breakdown simulation of electronegative gases in non-uniform field *J. Phys. D: Appl. Phys.* **18** 377
- Benilov M S and Naidis G V 2003 Modelling of low-current discharges in atmospheric-pressure air taking account of non-equilibrium effects *J. Phys. D: Appl. Phys.* **36** 1834–41
- Bityurin V A, Bocharov A N and Popov N A 2008 Numerical simulation of an electric discharge in supersonic flow *Fluid Dyn.* **43** 642–53
- Bourdon A, Pasko V P, Liu N Y, Célestin S, Ségur P and Marode E 2007 Efficient models for photoionization produced by non-thermal gas discharges in air based on radiative transfer and the Helmholtz equations *Plasma Sources Sci. Technol.* **16** 656–78
- Bourdon A, Bonaventura Z and Celestin S 2010 Influence of the pre-ionization background and simulation of the optical emission of a streamer discharge in preheated air at atmospheric pressure between two point electrodes *Plasma Sources Sci. Technol.* **19** 034012
- Celestin S, Bonaventura Z, Zeghondy B, Bourdon A and Ségur P 2009 The use of the ghost fluid method for Poisson's equation to simulate streamer propagation in point-to-plane and point-to-point geometries *J. Phys. D: Appl. Phys.* **42** 065203

- Demmel J W, Eisenstat S C, Gilbert J R, Li X S and Liu J W H 1999 A supernodal approach to sparse partial pivoting *SIAM J. Matrix Anal. Appl.* **20** 720–55
- Ferziger J and Peric M 2002 *Computational Methods for Fluid Dyn.* 3 edn (Berlin: Springer)
- Kulikovsky A A 1995 A More Accurate Scharfetter–Gummel algorithm of electron transport for semiconductor and gas discharge simulation *J. Comput. Phys.* **119** 149–55
- Kulikovsky A A 1997 Positive streamer between parallel plate electrodes in atmospheric pressure air *J. Phys. D: Appl. Phys.* **30** 441–50
- Liu N, Celestin S, Bourdon A, Pasko V P, Segur P and Marode E 2007 Application of photoionization models based on radiative transfer and the Helmholtz equations to studies of streamers in weak electric fields *Appl. Phys. Lett.* **91** 211501
- Maly R 1984 *Spark ignition: its physics and effect on the internal combustion engine* Fuel Economy in Road Vehicles Powered by Spark Ignition Engines ed J C Hilliard and G S Springer (New York: Plenum) pp 91–148
- Marode E 1975a The mechanism of spark breakdown in air at atmospheric pressure between a positive point and a plane: I. Experimental: nature of the streamer track *J. Appl. Phys.* **46** 2005–15
- Marode E 1975b The mechanism of spark breakdown in air at atmospheric pressure between a positive point and plane: II. Theoretical: computer simulation of the streamer track *J. Appl. Phys.* **46** 2016–20
- Marode E, Bastien F and Bakker M 1979 A model of the streamer-induced spark formation based on neutral dynamics *J. Appl. Phys.* **50** 140–6
- Mintoussov E I, Pendleton S J, Gerbault F G, Popov N A and Starikovskaia S M 2011 Fast gas heating in nitrogen-oxygen discharge plasma: II. Energy exchange in the afterglow of a volume nanosecond discharge at moderate pressures *J. Phys. D: Appl. Phys.* **44** 285202
- Mnatsakanyan A K and Naidis G V 1985 The vibrational energy balance in a discharge in air *High Temp.* **23** 506–13
- Morrow R and Lowke J J 1997 Streamer propagation in air *J. Phys. D: Appl. Phys.* **30** 614–27
- Naidis G 1999 Simulation of streamer-to-spark transition in short non-uniform air gaps *J. Phys. D: Appl. Phys.* **32** 2649–54
- Naidis G V 2005 Dynamics of streamer breakdown of short non-uniform air gaps *J. Phys. D: Appl. Phys.* **38** 3889
- Naidis G V 2008 Simulation of spark discharges in high-pressure air sustained by repetitive high-voltage nanosecond pulses *J. Phys. D: Appl. Phys.* **41** 234017
- Naidis G V 2009 Simulation of streamer-induced pulsed discharges in atmospheric-pressure air *Eur. Phys. J. Appl. Phys.* **47** 22803
- Pai D Z 2011 Nanomaterials synthesis at atmospheric pressure using nanosecond discharges *J. Phys. D: Appl. Phys.* **44** 174024
- Pai D Z, Stancu G D, Lacoste D A and Laux C O 2009 Nanosecond repetitively pulsed discharges in air at atmospheric pressure—the glow regime *Plasma Sources Sci. Technol.* **18** 045030
- Pai D Z, Lacoste D A and Laux C O 2010a Transitions between corona, glow, and spark regimes of nanosecond repetitively pulsed discharges in air at atmospheric pressure *J. Appl. Phys.* **107** 093303
- Pai D Z, Lacoste D A and Laux C O 2010b Nanosecond repetitively pulsed discharges in air at atmospheric pressure—the spark regime *Plasma Sources Sci. Technol.* **19** 065015
- Pancheshnyi S 2005 Role of electronegative gas admixtures in streamer start, propagation and branching phenomena *Plasma Sources Sci. Technol.* **14** 645–53
- Pilla G, Galley D, Lacoste D A, Lacas F, Veynante D and Laux C O 2006 Stabilization of a turbulent premixed flame using a nanosecond repetitively pulsed plasma *IEEE Trans. on Plasma Sci.* **34** 2471–7
- Popov N A 2001 Investigation of the mechanism for rapid heating of nitrogen and air in gas discharges *Plasma Phys. Rep.* **27** 886–96
- Popov N A 2011a Fast gas heating in a nitrogen-oxygen discharge plasma: I. Kinetic mechanism *J. Phys. D: Appl. Phys.* **44** 285201
- Popov N A 2011b Kinetic processes initiated by a nanosecond high-current discharge in hot air *Plasma Phys. Rep.* **37** 807–15
- Riourset J A, Pasko V P and Bourdon A 2010 Air density dependent model for analysis of air heating associated with streamers, leaders, and transient luminous events *J. Geophys. Res.* **115** A12321
- Rusterholtz D L 2012 Nanosecond repetitively pulsed discharges in atmospheric pressure air *PhD Thesis* Ecole Centrale Paris France
- Rusterholtz D L, Pai D Z, Stancu G D, Lacoste D A and Laux C O 2012 Ultrafast heating in nanosecond discharges in atmospheric pressure air *50th AIAA Aerospace Sciences Meeting including the New Horizons Forum and Aerospace Exposition (Nashville, TN January, 2012)* AIAA-2012-0509
- Shu C-W 1997 Essentially non-oscillatory and weighted essentially non-oscillatory schemes for hyperbolic conservation laws *NASA/CR-97-206253, ICASE Report No 97-65*
- Starikovskaia S M 2006 Plasma assisted ignition and combustion *J. Phys. D: Appl. Phys.* **39** R265
- Starikovskii A Y, Nikipelov A A, Nudnova M M and Roupassov D V 2009 SDBD plasma actuator with nanosecond pulse-periodic discharge *Plasma Sources Sci. Technol.* **18** 034015
- Tholin F 2012 Numerical simulation of nanosecond repetitively pulsed discharges in air at atmospheric pressure: application to plasma-assisted combustion *PhD Thesis* Ecole Centrale Paris, France
- Tholin F and Bourdon A 2011 Influence of temperature on the glow regime of a discharge in air at atmospheric pressure between two point electrodes *J. Phys. D: Appl. Phys.* **44** 385203
- Tholin F and Bourdon A 2013 Simulation of the stable ‘quasi-periodic’ glow regime of a nanosecond repetitively pulsed discharge in air at atmospheric pressure *Plasma Sources Sci. Technol.* **22** 045014
- Tholin F, Rusterholtz D L, Lacoste D A, Pai D Z, Celestin S, Jarrige J, Stancu G D, Bourdon A and Laux C O 2011 Images of a nanosecond repetitively pulsed glow discharge between two point electrodes in air at 300 K and at atmospheric pressure *IEEE Trans. Plasma Sci.* **39** 2254–55
- van Leer B 1979 Towards the ultimate conservative difference scheme: V. A second-order sequel to Godunov’s method *J. Comput. Phys.* **32** 101–36
- Vitello P A, Penetrante B M and Bardsley J N 1994 Simulation of negative-streamer dynamics in nitrogen *Phys. Rev. E* **49** 5574–98
- Xu D A, Lacoste D A, Rusterholtz D L, Elias P-Q, Stancu G D and Laux C O 2011 Experimental study of the hydrodynamic expansion following a nanosecond repetitively pulsed discharge in air *Appl. Phys. Lett.* **99** 121502